Research Article | Vol. 29, No. 9 / 26 April 2021 / Optics Express 12772
Optics EXPRESS

cSPARCOM: Multi-detector reconstruction by confocal super-resolution correlation microscopy

URI ROSSMAN,[1] TALI DADOSH,[2] YONINA C. ELDAR,[3] AND DAN ORON[1,*]

[1]Department of Physics of Complex Systems, Weizmann Institute of Science, Rehovot 7610001, Israel
[2]Department of Chemical Research Support, Weizmann Institute of Science, Rehovot 7610001, Israel
[3]Faculty of Mathematics and Computer Science, Weizmann Institute of Science, Rehovot 7610001, Israel
*dan.oron@weizmann.ac.il

Abstract: Image scanning microscopy (ISM), an upgraded successor of the ubiquitous confocal microscope, facilitates up to two-fold improvement in lateral resolution, and has become an indispensable element in the toolbox of the bio-imaging community. Recently, super-resolution optical fluctuation image scanning microscopy (SOFISM) integrated the analysis of intensity-fluctuations information into the basic ISM architecture, to enhance its resolving power. Both of these techniques typically rely on pixel-reassignment as a fundamental processing step, in which the parallax of different detector elements to the sample is compensated by laterally shifting the point spread function (PSF). Here, we propose an alternative analysis approach, based on the recent high-performing sparsity-based super-resolution correlation microscopy (SPARCOM) method. Through measurements of DNA origami nano-rulers and fixed cells labeled with organic dye, we experimentally show that confocal SPARCOM (cSPARCOM), which circumvents pixel-reassignment altogether, provides enhanced resolution compared to pixel-reassigned based analysis. Thus, cSPARCOM further promotes the effectiveness of ISM, and particularly that of correlation based ISM implementations such as SOFISM, where the PSF deviates significantly from spatial invariance.

1. Introduction

Super-resolution imaging enables the visualization of sub-diffraction limited objects, and has become an invaluable tool in the study of biology [1,2]. High-end prevailing modalities, such as stochastic optical reconstruction microscopy (STORM) [3], photo-activated localization microscopy (PALM) [4] and stimulated emission depletion (STED) [5], offer a significant gain in resolution that inevitably goes hand in hand with added experimental complexity, e.g. in the optical setup, sample preparation and imaging conditions. Other techniques, such as structured illumination microscopy [6] strive to achieve a more modest resolution improvement, with only little compromise on ease of implementation. A recent addition to this class of techniques is image scanning microscopy (ISM) [7,8]. Essentially, ISM relies on the ubiquitous architecture of a confocal microscope, but replaces the bucket detector with a pixelated one, where each pixel in the array acts as a sub-diffraction limited pinhole in a confocal scanning laser microscope. Consequently, the integrated response of the entire array can be analyzed to yield enhanced transverse resolution without any loss of signal. ISM has been incorporated into commercial products [9], and has become a successful robust technique for the bio-imaging community [10]. The core concept of ISM is the basis for numerous upgrades, extending further its capabilities. Examples include all optical realizations [11,12], point spread function (PSF) engineering [13,14] and multiphoton excitation [15–17]. Furthermore, ISM has been hybridized with different

#418422 https://doi.org/10.1364/OE.418422
Journal © 2021 Received 23 Dec 2020; revised 24 Mar 2021; accepted 26 Mar 2021; published 12 Apr 2021

Optics EXPRESS

imaging contrast mechanisms such as fluorescence lifetime [18], Raman scattering [19] and photon antibunching [20,21].

Recently introduced, a method called 'SOFISM' merged classical correlation information in the photon stream, the contrast agent used in super-resolution optical fluctuation imaging (SOFI [22]), with an ISM microscope to further enhance its transverse and axial resolution [23]. Essentially, since in ISM every detector pixel sees the object at a slightly different parallax, rather than summing the detected signal from all pixels as in a standard confocal microscope, the contributions from different pixels are first shifted to account for the parallax and then summed. This process is termed 'pixel-reassignment'.

The inherent assumption when performing pixel-reassignment is that the PSF is nearly spatially invariant. While this assumption is fulfilled in most ISM implementations, any deviation thereof implies room for improvement in imaging performance. Upgrading the reassignment process, which is equivalent to PSF averaging, to account for Stokes-shift, deviations from a Gaussian profile, aberrations and other imaging conditions, might include assignment of adaptive shift vectors to individual images [17,18,24,25]. Clearly, for SOFISM, which corresponds to correlation-enhanced ISM, there is a significantly larger algorithmic component entailed in the analysis of the correlation information. Furthermore, the assumption of spatial invariance is far from being correct for any realistic PSF, since the functional form of a multiplication of the PSF with its spatially shifted replica depends on the shift for most PSFs. Therefore, SOFISM analysis accentuates the spatial variance of the PSF, relative to standard ISM. In this work, we take advantage of ideas based on multi-measurement vector recovery and sparsity [26–28], to enhance the analysis of correlation information in ISM.

Sparsity-based signal recovery has become a valuable tool in many fields [27], including super-resolution imaging [29–36]. In [34] the authors developed a method named SPARCOM (sparsity-based super-resolution correlation microscopy), which relies on concepts from the field of sparse reconstruction, to algorithmically reconstruct super-resolved images out of fluorescence intensity fluctuations information in a wide-field microscope. It was shown that sparse recovery in the correlation domain, utilized in SPARCOM, extends the limits of image recovery from correlation information.

Following SPARCOM, here we extend the correlation-domain sparsity analysis to suit scanning microscopy modalities and name it 'confocal sparsity-based super-resolution correlation microscopy' (cSPARCOM). We discuss the relation between cSPARCOM and pixel-reassignment, and demonstrate that the naturally accentuated PSF spatial variance in scanning microscopy enhances the advantage of cSPARCOM analysis. Strictly speaking, we aim to retrieve augmented reconstructions of the underlying fluorescent objects in a confocal scan by formulating a convex optimization problem which utilizes sparsity in the correlation domain. Remarkably, our approach provides a means to improve on the process of pixel-reassignment, through bypassing the very process itself. We show that cSPARCOM is capable of obtaining resolution-enhanced reconstructions, and implement it first on simulated data, and subsequently on experimental data from scans of DNA origami nano-rulers, resolving features down to less than 100 *nm*. Finally, we implement cSPARCOM on experimental data acquired in scans of fixed cells labelled with ATTO 647N. Our results demonstrate that cSPARCOM is capable of resolving fine spatial detail which are obscured in pixel-reassignment based analysis.

2. ISM correlations and multi-detector reconstruction

In the following, we describe the empirical acquisition of temporal correlation information in a confocal microscope, and the concept lying at the basis of cSPARCOM analysis.

The experimental setup is essentially a realization of an ISM microscope with fast detectors, capable of probing fast fluorescence fluctuations, with a characteristic time of up to a few tens of microseconds (described in detail in Supplement 1). A fluorophore-labeled object is scanned

Optics EXPRESS

through a tightly focused laser beam, and the emitted fluorescence is collected, filtered and imaged onto a pixelated detector whose overall size spans approximately one Airy unit (AU), as depicted in Fig. 1(a). The pixelated detector consists of a fiber-bundle that guides the light to 14 individual single photon avalanche detectors (SPADs). The SPADs are connected to a time-correlated single-photon counting (TCSPC) card that records the arrival times of the incoming photons [37]. The SPADs and TCSPC high temporal resolution (sub-nanosecond) oversamples the fluorescence intensity fluctuations, and in fact temporal binning is carried out in post processing.

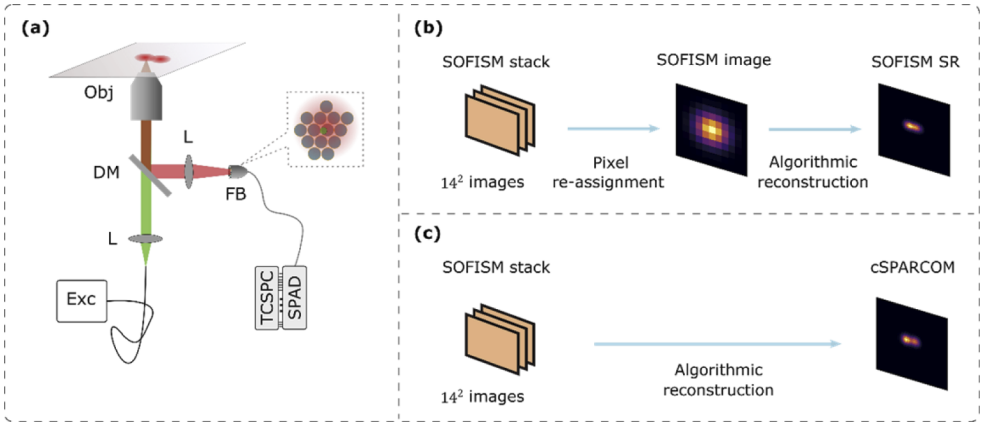

Fig. 1. Data acquisition and analysis schemes. (a) Optical setup. The standard pinhole in a confocal microscope is replaced by a fiber-bundle (FB), routing the fluorescent light to 14 individual SPADs. Exc, excitation laser; L, lens; DM, dichroic mirror; Obj, objective lens; Inset shows the facet of the fiber-bundle. The green dot represents the intersection of the optical axis with the image plane. (b) SOFISM SR image reconstruction procedure. Second-order correlation is calculated between all combinations of detector pairs to yield a stack of 14^2 images. An intermediate SOFISM image is created using pixel-reassignment processing, followed by application of a SR algorithm. (c) cSPARCOM image reconstruction procedure. The stack of correlation images is formed in the same manner as in (b). A similar SR algorithm, only modified to address the exclusion of pixel-reassignment, is used to reconstruct an image directly from the raw image stack.

The fact that each pixel is much smaller than the imaging PSF grants ISM lateral resolution gain, up to a factor of two over the diffraction limit [8]. A useful way to illustrate the source of resolution improvement is to consider the probability to detect a signal from emitters in the object. In ISM, signal detection comprises the probability to excite an emitter, and the probability to detect its emitted fluorescence, which amounts to multiplication of the excitation and imaging PSFs, leading to a narrower effective PSF. SOFISM extends the capabilities of standard ISM by analyzing temporal intensity fluctuations (blinking), naturally occurring in practically all fluorescent emitters, rather than their integrated intensity value [23]. The key ingredient is that fluorescent emitters blink independently from one another, excluding adjacent emitters which might be affected by short-range inter-molecule interactions. As a result, calculating the n^{th} order statistics of the intensity holds the potential to an $\sqrt{n}$-fold resolution improvement compared to the diffraction limit [22]. Furthermore, applying Fourier reweighting (deconvolution) one can in principle achieve an n-fold improvement. In this work we chose to focus on second-order correlations in fluorescence fluctuations, although the ideas presented here, may be applied to higher correlation orders. The resolution improvement in second-order SOFISM is therefore the merger of two contributions, blinking and ISM, enabling up to four-fold resolution improvement over the diffraction limit. Attributing the resolution enhancement of SOFISM to the multiplication

Optics EXPRESS

of native PSFs, the resulting PSF is composed of a multiplication of two ISM PSFs, representing the correlation between pairs of detectors, or the auto-correlation of a detector with itself.

Pixel-reassignment is an integral part of ISM modalities: Indeed, resolution is enhanced owing to the fact that each detector is much smaller than the PSF, nonetheless only a small fraction of the light is collected by it. In order to fully capitalize on the enhanced resolution, without a prohibitive degradation in the signal-to-noise ratio (SNR), the information from different detectors should be merged. Because each detector sees the imaged object at a different parallax, its recorded image features a respective spatial displacement. Thus, prior to summation, an adequate lateral shift correction needs to be applied to each image. In ISM, reassignment can be performed either in post processing or through all-optical realizations that alleviate the need for a fast detector array and multiple exposures [11,12]. In contrast, in SOFISM, due to the need to calculate correlations, pixel reassignment is implemented solely in post processing, using a straightforward generalization of pixel-reassignment to account for all combinations of detector pairs. However, as will be described in the next section, the very process of image summation via pixel-reassignment causes degradation of the fine details in the correlation image, due to the fact that the PSF in SOFISM is far from being spatially invariant.

In an effort to obtain enhanced super-resolved images, we propose an alternative approach to analyze SOFISM scans, employing a sparsity-based reconstruction algorithm, and notably circumventing pixel-reassignment. Following a SOFISM scan, deconvolution can be performed in two distinct paths – either on pixel-reassigned data or on the raw data itself. The first is schematically shown in Fig. 1(b), and includes three main steps. Initially, it undertakes calculation of correlation images from all detector pairs. This is then followed by formation of a SOFISM image, through a pixel-reassignment process. Finally, it involves implementing a sparse reconstruction (SR) optimization algorithm on the pixel-reassigned image. In contrast, the second path, depicted in Fig. 1(c), is comprised of only two stages. While calculation of the stack of correlation images is identical, it is now followed directly by application of a modified SR algorithm, cSPARCOM. Notably, we skip the intermediate step of generating a SOFISM image by pixel-reassignment. It is important to mention that, in order to make a meaningful valid comparison, the altered algorithm leaves the underlying type of optimization problem unchanged; it only introduces an adaptation accounting for the fact that no pixel-reassignment was performed. While these paths may seem, at first sight, perfectly interchangeable, careful inspection of the role of pixel-reassignment shows that these two schemes are not equivalent. As a matter of fact, the method in Fig. 1(c) exhibits greater potential for resolution improvement relative to that in Fig. 1(b). The next section explores a secondary effect of pixel-reassignment processing, unveiling a resolution improvement source, which we harness in our approach.

3. Exploiting PSF variations to enhance resolution

In scanning microscopy, the effective PSF pertaining to each detector depends on its position with respect to the optical axis. This can readily be understood by recalling that the spatial profile of the PSF corresponds to multiplication of the native PSFs, the excitation and the detection one. In general, the shape of a multiplication of functions need not be invariant to relative shifts between them. A special case is the multiplication of two Gaussians, which maintains its functional profile up to a multiplicative factor, regardless of their relative position. Even though a Gaussian approximation of the PSF is predominantly useful and convenient, when considering the fine detail, the deviations from a Gaussian shape become significant. In the case of circular-aperture optics, a more accurate model of the PSF is an Airy disk. Consequently, different detectors are characterized by varying PSFs, as illustrated in Fig. 2. Panel (2.a) presents an exemplary assortment of ISM PSFs of point-like detectors at different distances from the optical axis, where the imaging system is characterized by an Airy shaped PSF. These PSFs are formed by multiplying the laser excitation PSF with the detection PSF of each detector. It

Optics EXPRESS

is clearly evident that the greater the distance between the detector and the optical axis, the more distorted and asymmetric its PSF profile. In addition, the relative amplitudes of the PSFs express the fact that detectors far from the optical axis naturally collect less light, and their overall contribution is less dominant than detectors which are near the optical axis.

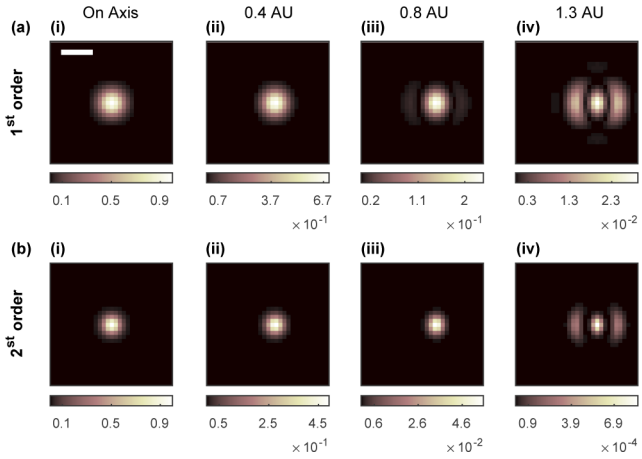

Fig. 2. Variations of the PSF in scanning microscopy. (a) First order PSFs of detectors at various distances from the optical axis: (i) On axis detector; (ii) 0.4 AU; (iii) 0.8 AU; (iv) 1.3 AU. PSFs in (a) were normalized to the highest value in (a-i); (b) Second order auto-correlation PSFs of the same detectors as in (a). (i) On axis detector; (ii) 0.4 AU; (iii) 0.8 AU; (iv) 1.3 AU. PSFs in (b) were normalized to the highest value in (b-i); Scale bar: 1 AU.

Similarly, second-order correlation SOFISM PSFs are comprised of multiplication of three of the native system PSFs, one of the excitation squared, and two of detection. Alternatively, one can think of second-order SOFISM PSFs as the multiplication of two ISM PSFs. Panel (2.b) portrays profile variations in SOFISM PSFs, corresponding to the auto-correlation of detectors located at the same positions as in panel (2.a). We note that many other PSF shapes occur, upon considering cross-correlation between pairs of detectors, rather than a single detector's auto-correlation. The former involves multiplication of two distinct ISM PSFs, whereas the latter involves a single ISM PSF squared. In the interest of simplicity, panel (2.b) includes examples of single detector auto-correlation PSFs only.

Figure 2 intuitively establishes the reason why pixel-reassignment of the image stack leads to loss of information in the final image [25,38]. Essentially, every image in the stack is characterized by a slightly different blurring, dictated by its PSF. As a result, translation and summation of different images, amounts to averaging images which are blurred in different ways. In particular, fine details originally present in each raw image, can become obscured due to this averaging process, impairing the resolution of the final image. An upgraded scheme for image summation is called adaptive pixel-reassignment [22–25]. Even though adaptive pixel-reassignment does not eliminate PSF averaging, it achieves improved results, as compared with, for example, the all-optical reassignment methods, which feature a predetermined shift vector [11,12,15].

cSPARCOM bypasses PSF averaging and takes advantage of the various PSF shapes naturally occurring in SOFISM measurements, to improve the resolution of the final image. In principle, we alleviate the need for pixel-reassignment using the approach of algorithmic fusion of individual images with complementary properties (see for example [35,39,40]). More specifically, we incorporate the inherent PSF variations into a sparsity-based algorithm, and achieve enhanced reconstructions from both simulated and experimental measurements. We further revisit the

Optics EXPRESS

SPARCOM algorithm for wide-field images and note that it too circumvents pixel-reassignment which is usually performed in SOFI when assigning the correlation signal between different pixels to new 'virtual' pixels [22]. In the case of wide-field SOFI and SPARCOM, the significance of PSF averaging is relatively minor since the effective PSFs are comprised of a multiplication of only two detection PSFs. However, in SOFISM and cSPARCOM, the effective PSFs are comprised of a multiplication of four PSFs, two of the excitation PSF and two detection PSFs. Consequently, the spatial variance of the PSFs in cSPARCOM is more pronounced, thus enhancing the benefit of circumventing pixel-reassignment.

4. Reconstruction algorithms

In the following section we describe the two analysis algorithms, corresponding to Figs. 1(b)-(c). Essentially, these algorithms are used to computationally reconstruct the underlying object of interest out of the measured data. This is achieved by formulating and solving an appropriate optimization problem which encompasses the imaging process and prior knowledge about the properties of the object.

4.1. SOFISM SR

We start with standard image SR, which serves as a means for comparison for the cSPARCOM algorithm, presented subsequently. Consider the setting depicted in Fig. 1(b). In the framework of image SR, one aims to recover a high resolution $N \times N$ image, from a low resolution $M \times M$ image, where $M<N$. The image is mathematically modeled by a discrete linear system $\boldsymbol{y} = \boldsymbol{A}\boldsymbol{x}+\boldsymbol{n}$. The vector $\boldsymbol{y}^{M^2\times 1}$ is a column stacking of the measured image, $\boldsymbol{n}^{M^2\times 1}$ is unknown noise, and the vector $\boldsymbol{x}^{N^2\times 1}$ is the high resolution image to be estimated. The matrix $\boldsymbol{A}^{M^2\times N^2}$ is a known blurring operator, its columns being subpixel shifted copies of the PSF of the imaging system. Reconstruction means solving an optimization problem, namely minimizing a cost function, in order to retrieve the 'true' deblurred object $\boldsymbol{x}$.

Importantly, since the number of measurements M^2 is smaller than the number of variables N^2, generally one needs to regularize the solution in order to obtain a meaningful recovery. A very powerful approach in super-resolution imaging, and compressed sensing in general, is to enforce sparsity in the solution, meaning that only a small percentage of its elements are non-zero [27,28]. The requirement for sparsity in some basis representation is a very prevalent property in nature [29,41]. Utilization of the l_1 norm as a measure for sparsity, alongside a least squares data fidelity term, leads to the well known convex optimization problem

$$\underset{\boldsymbol{x}}{\text{minimize}}\ \{||\boldsymbol{A}\boldsymbol{x}-\boldsymbol{y}||_2^2+\lambda||\boldsymbol{x}||_1\}, \tag{1}$$

where $||\cdot||_2$ denotes the l_2 norm, $||\cdot||_1$ is the l_1 norm, and $\lambda \geq 0$ is a regularization parameter.

In the setting shown in Fig. 1(b), $\boldsymbol{y}$ represents the pixel-reassigned SOFISM image, and the constituent PSF of $\boldsymbol{A}$ corresponds to the averaged SOFISM PSF.

4.2. cSPARCOM

Next, we turn to consider the case where instead of forming a reassigned image we have a multiplicity of sub-images $\boldsymbol{y}_i$, the index i running through the image stack at our disposal. In addition to multiple images, we have their concomitant PSFs $\boldsymbol{A}_i$, as was elucidated earlier. In light of the above, we formulate the following revised convex optimization problem

$$\underset{\boldsymbol{x}}{\text{minimize}}\ \{\sum_{i=1}^{R}||\boldsymbol{A_i}\boldsymbol{x}-\boldsymbol{y_i}||_2^2+\lambda||\boldsymbol{x}||_1\}, \tag{2}$$

where R is the number of sub-images. The reconstruction problem expressed in Eq. (2) correlates with the diagram in Fig. 1(c), in which the raw image stack is input to the algorithm. In

Optics EXPRESS

this formulation, each image $\boldsymbol{y_i}$, originating from the correlation between a pair of detectors, contributes a separate term to the sum of least squares. Importantly, it enters the sum with its associated measurement matrix $\boldsymbol{A_i}$, that may encapsulate lateral shifts as well as shape distortions in the PSF. Clearly, the problems in Eq. (1) and Eq. (2) both represent optimization problems of a similar form. The substantial difference between them is, that the former handles the pixel-reassigned image, whereas the latter takes into account the original multiplicity of sub-images without pixel-reassignment. We note that in the case of a Gaussian PSF, the solution of Eq. (2) becomes equivalent to that of Eq. (1), since reassignment does not alter the shape of the resulting PSF.

The problem in Eq. (2) can be transformed to a more concise form, in the spirit of the work by Solomon et al. [34], where the authors exploited correlations in a widefield microscope through SPARCOM analysis. The equivalent representation is derived in detail in Supplement 1. Essentially in this alternative form of cSPARCOM, the temporal correlations between detectors are calculated as part of the algorithm, and not in a pre-processing stage. In turn, this simplifies the input to the algorithm. Relating to the optical setup used here, the input reduces to 14 detectors' time traces and PSFs, instead of 14^2 images and PSFs. Nevertheless, we chose to present the problem in its current form [Eq. (2)], inasmuch as it allows for a straightforward comparison to Eq. (1). We note, that both problems are solved using the fast iterative shrinkage-thresholding algorithm (FISTA) method [42,43] (see Supplement 1).

5. Simulation

We first examine cSPARCOM on simulated data, emulating a confocal scan of a known scene of stochastically fluctuating emitters (see Supplement 1). Figure 3(a) shows the ground truth for this scan, comprising a preset arrangement of emitters with variable-brightness, smoothened with a narrow Gaussian PSF. The resulting SOFISM image, is presented in Fig. 3(b). As described earlier, SOFISM image processing includes calculation of temporal correlations between all detector pairs, adequate pixel-reassignment, and summation of all contributing images. While some coarse structural details are already apparent in the SOFISM image, application of reconstruction algorithms is expected to yield an improved representation of the hidden ground truth. In Fig. 3(c) we applied cSPARCOM reconstruction on non pixel-reassigned data, according to Eq. (2). As a reference for the performance of cSPARCOM, we use the results of a standard image SR [see Eq. (1)], implemented on the processed SOFISM image [Fig. 3(d)]. Visually inspecting the reconstruction results in Figs. 3(c-d), we observe that cSPARCOM delivers a better representation of the ground truth than regular SOFISM SR. Even though both reconstructions share many similarities in either readily resolvable situations or challenging ones, cSPARCOM is able to resolve more emitters, at a borderline separation range of about $60-70$ nm, and to better estimate the distances between them. We conducted many such simulations, with different scene, noise and fluctuation realizations, and in all of them cSPARCOM performed at least as well as SOFISM SR. In the majority of cases, it obtained better results. As discussed earlier, pixel-reassignment prior to reconstruction is the only substantial difference between the two methods. Thus, we attribute the enhanced performance of cSPARCOM to its deliberate evasion of pixel-reassignment. Put differently, the simulation results in Fig. 3 demonstrate that the common practice of pixel-reassignment in correlation microscopy is accompanied by some loss of information, which otherwise can be accessible through alternative analysis. Although the resolution gain potential is modest, it nevertheless reaches to the extent where it bears discernible differences in algorithmic reconstructions.

We conclude this section with a discussion on the effect of PSF averaging on ISM reconstructions. Purportedly, the negative effect of PSF averaging on SOFISM is expected to hamper ISM image reconstruction in an analogous manner. Likewise, if we were to exploit the different PSFs in ISM [see Fig. 2(a)] and bypass pixel-reassignment in the reconstruction, we might similarly harvest

Optics EXPRESS

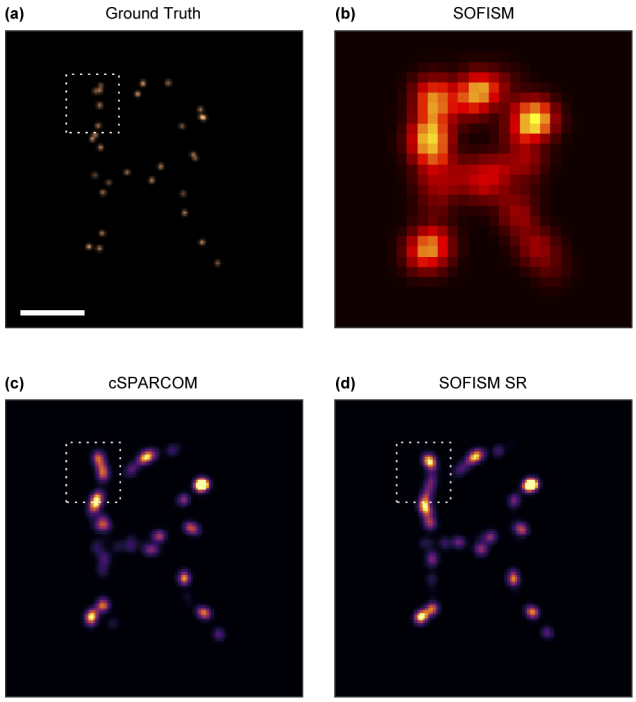

Fig. 3. Performance of cSPARCOM and standard SOFISM SR algorithms on simulated data. (a) Ground truth of a scene of emitters. (b) SOFISM image analyzed from a scan featuring 30 *ms* pixel dwell time and 40 *nm* step size. (c) cSPARCOM reconstruction of correlation image stack (not shown). (d) SR reconstruction implemented on (b). Marked frames designate an area where cSPARCOM resolves more particles than SOFI SR. Scale bar, 250 *nm*.

the hidden resolution potential. Therefore, based on Eq. (2), we ran algorithmic reconstructions, where correlation sub-images and PSFs were substituted by intensity images recorded by the individual detectors, and their corresponding PSFs. We refer to this type of reconstruction as multi-detector ISM SR. Finally, we compared multi-detector ISM SR to regular ISM SR, the latter following Eq. (1). Surprisingly nonetheless, repeated simulations showed no substantial difference in the performance of the two algorithms. We strongly believe, that the reason for the lack of discernable improvement in multi-detector ISM SR is rooted at the distribution of energy among the different PSFs. In ISM, a large portion of the light is divided between few central detectors, exhibiting marginally different PSF shapes. In contrast, in the case of correlation between detectors, the same amount of light is distributed between a much larger variety of PSF shapes, featuring greater distortions, since they are constructed from multiplication of two ISM PSFs. Thus, the overall effect of PSF inhomogeneity in SOFISM is accentuated, reinforcing the potential resolution gain to a significant level.

5.1. Sparsity in different domains

The fundamental principle of exploiting different PSF shapes in confocal measurements can be implemented using alternative types of regularizers, other than the l_1 norm (i.e. sparsity assumption in the positions of the emitters) in the basic formulation appearing in Eq. (2). The choice of a suitable regularizer depends on the prior knowledge about the object. In particular, since most natural images are found to be sparse in some basis representation [29,41], one might exploit sparsity in other domains, and not necessarily in the emitter-position domain. In the

Optics EXPRESS

case of a densely labeled sample, involving more continuous filaments, assuming sparsity in the wavelet domain can prove beneficial, and assist in recovering an image that represents better the real object. In what follows, we explore the application of cSPARCOM on simulated data, assuming sparsity in the wavelet domain. We utilize a Daubechies wavelet decomposition of order two with eight taps (see [44] for details). The ground truth in the simulation is two 400 *nm*-long parallel strands, with 20 *nm* separation between consecutive emitters. The distance between the lines is 95 *nm*. Panel (a) of Fig. 4 shows the ISM image, superimposed with the ground truth locations of the emitters, and panel (b) presents the SOFISM image. Reconstructions utilizing sparsity in the wavelet domain are shown in panels (c)-(d). For reference, panels (e)-(f) present reconstructions assuming sparsity in the emitter-position domain (according to Eq. (1) and (2)). Comparing the four reconstructions, we see that wavelet-based recovery produces smoother, less grainy super-resolved images, compared to l_1-based recovery. Most importantly, observing panels (c) and (d), we see that cSPARCOM yields a better reconstruction than SOFISM SR. In particular, cSPARCOM manages to resolve the right end of the underlying structure, and exhibits an overall slightly sharper image. This example, though somewhat simplistic, illustrates that in some cases, assuming sparsity in domains other than the original emitter-position domain may help produce reconstructions which are more faithful to the underlying object and have smoother textures.

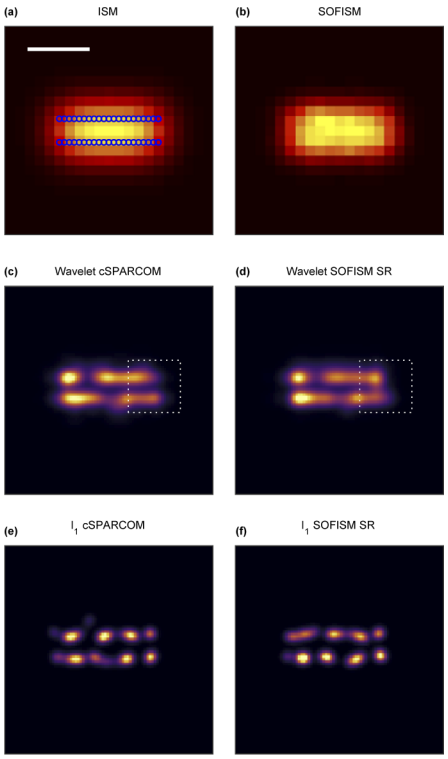

Fig. 4. Performance of cSPARCOM and standard SOFISM SR algorithms on simulated densely labeled lines, utilizing sparsity in the wavelet domain. (a) ISM image with overlaid emitter positions (blue circles); distance between the lines is 95 *nm*. (b) SOFISM image. (c)-(d) Wavelet reconstructions (sparsity in the wavelet domain): (c) cSPARCOM; (d) SOFISM SR. (e)-(f) l_1 reconstructions (sparsity in the emitter-position domain): (e) cSPARCOM; (f) SOFISM SR. Marked frames designate a region where cSPARCOM manages to resolve better than SOFISM SR. Scale bar, 250 *nm*.

Optics EXPRESS

6. Experimental results

We continue and demonstrate cSPARCOM reconstruction from experimental data, obtained in scans of samples labelled with the fluorescent dye Atto 647N. In general, in order to facilitate viable fluctuation based super-resolution microscopy, one has to utilize an appropriate fluorophore and control the statistics of transitions between emissive states ('on') and dark states ('off'), by carefully tailoring the imaging conditions, such as imaging buffer, laser power, and often the use of additional light sources that induce photoswitching [45–47]. The use of self-blinking dyes decouples the blinking properties from the illumination and can substantially simplify SOFI imaging [48]. Typically, in wide-field SOFI applications the frame exposure time is a few tens of milliseconds, and should roughly match the characteristic 'on' time of the fluorophore [22,48–51]. Thus, a typical wide-field SOFI measurement, which involves the acquisition of a sequence of tens or hundreds of wide-field images would lead to yet acceptable prolonged exposure times. In contrast, in scanning microscopy, where the measurement is performed pixel-by-pixel, the required long exposure times would render the measurement completely impractical. However, utilizing the high sensitivity and temporal resolution of our fiber-bundle single-photon camera, we were able to take advantage of fast intensity intermittencies, occurring at the sub millisecond level [52], and obtain moderate SNR images with pixel dwell time of 30 *ms*. Contrary to wide-field SOFI applications, we tried to suppress long intermittencies, since these could not have been estimated well within the time frame of a confocal scan. Notably, no specialized measures were necessary for tuning the blinking of Atto 647N dye molecules. Instead, we employed a rather broad application antifade buffer (Prolong Gold/Glass, Invitrogen) to enhance photo stability, and lessen photo-bleaching. Importantly, although the fluorophores showed stable emission averaged over time scales of a wide-field EMCCD frame rate, fast fluctuations persisted, and could be accessed in our experimental setup.

6.1. Resolution tests with nano rulers

In order to empirically investigate the potential advantages of cSPARCOM close to the resolution limit, we conducted scans of DNA origami nano-rulers (GattaQuant) labelled with 2-4 Atto 647N molecules at each emitting point, and mounted in 'Prolong Gold Antifade Mountant' (Invitrogen). The rulers fulfilled the role of a ground truth for the measurements. Figure 5 presents the results obtained from measurements of nano-rulers of three different types. ISM images are shown as well for reference, although they take no part in the algorithmic reconstructions. Panels 5(a)-(b) show, respectively, the ISM and SOFISM images analyzed from the scan of two-site rulers with 160 *nm* separation between their emitting sites. We used adaptive pixel-reassignment, as the shift vectors were derived from a calibration measurement of a single fluorescent bead (see Supplementary of [23]). The calibration measurement was also used to estimate the PSFs required for the following algorithmic reconstructions, as shown in Supplement 1. While the SOFISM image is noisier, it already discloses the structure of the scene, unlike the ISM image. The composition of the underlying object is fully unraveled in Figs. 5(c) and 5(d), corresponding to the reconstruction results of cSPARCOM and ordinary SOFISM SR, using l_1 norm as the measure for sparsity. Both reconstructions retrieve two rulers with approximately 160 *nm* separation between their ends. Certainly, the molecules within each end are too close to each other to resolve in any of the methods discussed here. Nonetheless, the reconstructions seem to perform just as well, not showing any conspicuous differences. More challenging scenes are shown in the middle and right panels of Fig. 5. The optical images in Figs. 5(e) and 5(f) were processed from a scan of two-site 100 *nm* rulers, while those in .Figs. 5(i) and 5(j) correspond to three-site 200 *nm* rulers, with 100 *nm* spacing between emitting points. We comment that, because the fluorescent labeling is stochastic, both ends of a ruler might differ in brightness, imposing additional difficulty to resolve them. Yet, visually comparing Figs. 5(g)-(h) and 5(k)-(l), we observe that in these demanding settings, cSPARCOM manages to outperform SOFISM

Optics EXPRESS

SR. Even though some features remain obscure, cSPARCOM is able to recover more rulers with emitting-site separation in the range of 85 – 100 *nm*, in excellent agreement with samples properties (see [53] for length distribution in DNA origami nano-rulers).

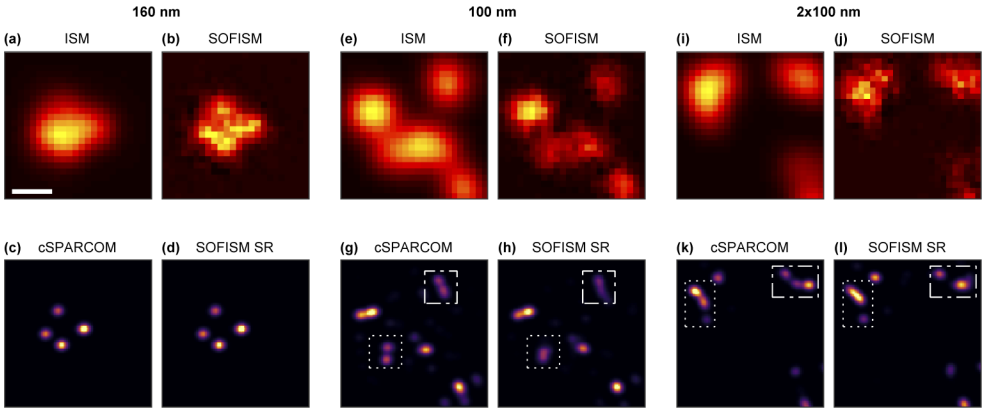

Fig. 5. Nano-rulers measurements and l_1 based reconstructions. Left panel, (a)-(d), results from a scan of two-site 160 *nm* rulers. (a) ISM image; (b) SOFISM image; (c) cSPARCOM; (d) SR of SOFISM image in (b). Middle panel, (e)-(h), results from a scan of two-site 100 *nm* rulers. (e) ISM image; (f) SOFISM image; (g) cSPARCOM; (h) SR of SOFISM image in (f). Right panel, (i)-(l), results from a scan of three-site 200 *nm* rulers, with 100 *nm* spacings. (i) ISM image; (j) SOFISM image; (k) cSPARCOM; (l) SR of SOFISM image in (j). Marked frames highlight nano-rulers which cSPARCOM resolves better than SOFISM SR. Scans featured a 40 *nm* step size and a 30 *ms* pixel dwell time. Scale bar, 250 *nm*.

6.2. *Microtubules in fixed cells*

Finally, to show the applicability of cSPARCOM in bio-imaging, we demonstrate its use in measurements of a sample of fixed HeLa cells, whose microtubules were labelled with Atto 647N (see Supplement 1). We note that the labeling density had to be tuned, such as to avoid saturation of the SPAD detectors. The sample was mounted with 'ProLong Glass Antifade Mountant' (Invitrogen). Figure 6 shows the ISM image [6(a)], SOFISM image [6(b)], together with cSPARCOM and SOFISM SR l_1 and wavelet reconstructions [6(c-f)], corresponding to a typical scene in the object. Here, the reconstructions cannot be compared based on a ground truth. Yet, we can obtain some insight by concentrating on situations where features are at least nearly resolved in all reconstructions. These settings serve as common ground for comparison since all algorithms imply more than a single emitter. Although the object itself is somewhat grainy, due to the necessary low concentration labeling, it seems that the l_1 based reconstructions tend to recover overly grainy-appearance images. Nevertheless, the wavelet reconstructions appear smoother and better capture the width of the filaments. While in some locations SOFI SR seems to perform better, in most cases however, cSPARCOM is able to better resolve details, as exemplified in the insets in Figs. 6(e)-(f).

Optics EXPRESS

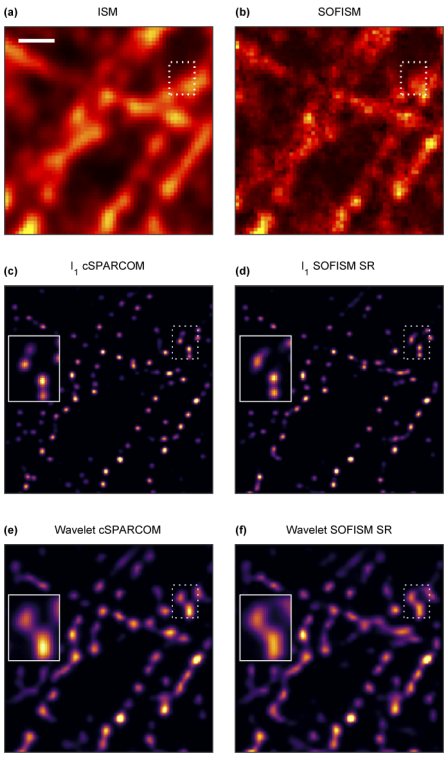

Fig. 6. Measurement and reconstruction of microtubules in a fixed cell sample. (a)-(f), Images analyzed from a confocal scan (50 *nm* step size and 30 *ms* pixel dwell time) of a fixed HeLa cell, labeled with Atto 647N. (a) ISM image. (b) SOFISM image. (c) cSPARCOM l_1 reconstruction. (d) l_1 SR of the SOFISM image in (b). (e) cSPARCOM wavelet reconstruction. (f) Wavelet SR of the SOFISM image in (b). Solid-line inset is a magnification of the area in the dotted-frame. Scale bar, 0.5 μm.

7. Discussion and conclusions

We demonstrated cSPARCOM algorithmic reconstruction of SOFISM scans utilizing the fastest switching dynamics of organic dyes, mostly 'invisible' to widefield EMCCDs [52]. By circumventing standard pixel-reassignment, we were able to extract fine-feature spatial information that would have been otherwise lost, due to PSF averaging. Thus, cSPARCOM stretches the resolution boundaries of correlation-enhanced ISM microscopes, markedly at no expense other than the reconstruction being computationally more demanding. The concept of alleviating the need for pixel-reassignment in multi-detector imaging is not limited to sparsity in the emitter-position domain, nor to sparsity-based reconstructions in general, but can be used in other types of optimization problems and correlation analysis methods [39,44,54–59].

cSPARCOM is practical even with straightforward imaging conditions. Nevertheless, special attention must be given to the choice of fluorophore, as the interplay between brightness, photostability and photobleaching is essential for maintaining a relatively short pixel dwell time along with sufficient signal level. In particular, care should be taken to minimize photobleaching, which may introduce a false positive correlation contrast, overwhelming the genuine correlations associated with fluorescence intermittencies. In addition, since we rely on the fastest triplet blinking in fluorophores, photostability of the fluorophore is favored upon prolonged blinking periods. Although in this work no specialized measures, other than a commercial antifade reagent,

Optics EXPRESS

were employed, we believe that some optimization of the on-off switching, through adjustment of imaging buffer and excitation, could improve the SNR. In addition, in order to avoid saturation of the SPADs, the labeling density of the samples had to be adjusted to a lower level than what is typically used in imaging systems that employ less sensitive detectors. Finally, since triplet dark state blinking ranges typically between a few microseconds up to a millisecond [52], the highest temporal resolution available with SPADs is not imperative. Therefore, other types of fast detectors can be utilized, for instance a PMT array, relaxing labeling concentration, computer memory and processing time requirements.

We strongly believe that pixel dwell time could be diminished using advanced algorithmic analysis (see for example [35]). However, because cSPARCOM exploits the information from outer rim detectors, low SNR might limit their contribution, even though the overall image SNR is still reasonable. Nevertheless, in this degenerate case, cSPARCOM is expected to perform at least as well as image SR, and thus could still serve as the default reconstruction path.

According to our simulations, bypassing pixel-reassignment did not show any pronounced improvement when applied to the basic form of intensity-based ISM consisting of a ~1 AU detector array. However, when implemented on second-order correlations, cSPARCOM exhibited conspicuous differences compared to image SR. We speculate that extension of this idea to higher orders can emphasize the effect, as the fluorescent light would be distributed between a greater number of distorted PSFs. Finally, we comment that rather than estimating multiple PSFs from a calibration measurement, deducing the PSFs directly from a measured scene, using tools from the area of machine learning, could potentially increase the method's performance and robustness, especially in cases where the sample is weakly scattering [36].

Funding. European Research Council (consolidator grant ColloQuantO); H2020 European Research Council (646804-ERC-COG-BNYQ); Crown Photonics Center; Minerva Foundation; KLA-TENCOR Corporation; Israeli Council for Higher Education (CHE) via the Weizmann Data Science Research Center.

Acknowledgements. The authors thank Nikita Kamenetsky for the preparation of biological samples. D. O. is the incumbent of the Harry Weinrebe Professorial Chair of Laser Physics.

Disclosures. A patent on the reported method has been submitted.

Supplemental document. See Supplement 1 for supporting content.

References

1. Y. M. Sigal, R. Zhou, and X. Zhuang, "Visualizing and discovering cellular structures with super-resolution microscopy," Science **361**(6405), 880–887 (2018).
2. D. Baddeley and J. Bewersdorf, "Biological Insight from Super-Resolution Microscopy: What We Can Learn from Localization-Based Images," Annu. Rev. Biochem. **87**(1), 965–989 (2018).
3. M. J. Rust, M. Bates, and X. Zhuang, "Sub-diffraction-limit imaging by stochastic optical reconstruction microscopy (STORM)," Nat. Methods **3**(10), 793–796 (2006).
4. E. Betzig, G. H. Patterson, R. Sougrat, O. W. Lindwasser, S. Olenych, J. S. Bonifacino, M. W. Davidson, J. Lippincott-Schwartz, and H. F. Hess, "Imaging Intracellular Fluorescent Proteins at Nanometer Resolution," Science **313**(5793), 1642–1645 (2006).
5. S. W. Hell and J. Wichmann, "Breaking the diffraction resolution limit by stimulated emission: stimulated-emission-depletion fluorescence microscopy," Opt. Lett. **19**(11), 780–782 (1994).
6. M. G. Gustafsson, "Surpassing the lateral resolution limit by a factor of two using structured illumination microscopy," J. Microsc. **198**(2), 82–87 (2000).
7. C. J. R. Sheppard, "Superresolution in confocal Imaging," Optik (Stuttg **80**(2), 53–54 (1988).
8. C. B. Müller and J. Enderlein, "Image scanning microscopy," Phys. Rev. Lett. **104**(19), 198101 (2010).
9. J. Huff, "The Airyscan detector from ZEISS: confocal imaging with improved signal-to-noise ratio and super-resolution," Nat. Methods **12**(12), i–ii (2015).
10. I. Gregor and J. Enderlein, "Image scanning microscopy," Curr. Opin. Chem. Biol. **51**, 74–83 (2019).
11. S. Roth, C. J. R. Sheppard, K. Wicker, and R. Heintzmann, "Optical photon reassignment microscopy (OPRA)," Opt. Nanoscopy **2**(1), 5–6 (2013).
12. G. M. R. De Luca, R. M. P. Breedijk, R. A. J. Brandt, C. H. C. Zeelenberg, B. E. de Jong, W. Timmermans, L. N. Azar, R. A. Hoebe, S. Stallinga, and E. M. M. Manders, "Re-scan confocal microscopy: scanning twice for better resolution," Biomed. Opt. Express **4**(11), 2644–2656 (2013).
13. C. Roider, R. Piestun, and A. Jesacher, "3D image scanning microscopy with engineered excitation and detection," Optica **4**(11), 1373–1381 (2017).

Optics EXPRESS

14. F. Strasser, M. Offterdinger, R. Piestun, and A. Jesacher, "Spectral image scanning microscopy," Biomed. Opt. Express **10**(5), 2513–2527 (2019).
15. I. Gregor, M. Spiecker, R. Petrovsky, J. Großhans, R. Ros, and J. Enderlein, "Rapid nonlinear image scanning microscopy," Nat. Methods **14**(11), 1087–1089 (2017).
16. O. Tzang, D. Feldkhun, A. Agrawal, A. Jesacher, and R. Piestun, "Two-photon PSF-engineered image scanning microscopy," Opt. Lett. **44**(4), 895–898 (2019).
17. S. V. Koho, E. Slenders, G. Tortarolo, M. Castello, M. Buttafava, F. Villa, E. Tcarenkova, M. Ameloot, P. Bianchini, C. J. R. Sheppard, A. Diaspro, A. Tosi, and G. Vicidomini, "Two-photon image-scanning microscopy with SPAD array and blind image reconstruction," Biomed. Opt. Express **11**(6), 2905–2924 (2020).
18. M. Castello, G. Tortarolo, M. Buttafava, T. Deguchi, F. Villa, S. Koho, L. Pesce, M. Oneto, S. Pelicci, L. Lanzanó, P. Bianchini, C. J. R. Sheppard, A. Diaspro, A. Tosi, and G. Vicidomini, "A robust and versatile platform for image scanning microscopy enabling super-resolution FLIM," Nat. Methods **16**(2), 175–178 (2019).
19. C. Roider, M. Ritsch-Marte, and A. Jesacher, "High-resolution confocal Raman microscopy using pixel reassignment," Opt. Lett. **41**(16), 3825–3828 (2016).
20. R. Tenne, U. Rossman, B. Rephael, Y. Israel, A. Krupinski-Ptaszek, R. Lapkiewicz, Y. Silberberg, and D. Oron, "Super-resolution enhancement by quantum image scanning microscopy," Nat. Photonics **13**(2), 116–122 (2019).
21. G. Lubin, R. Tenne, I. Michel Antolovic, E. Charbon, C. Bruschini, and D. Oron, "Quantum correlation measurement with single photon avalanche diode arrays," Opt. Express **27**(23), 32863–32882 (2019).
22. T. Dertinger, R. Colyer, G. Iyer, S. Weiss, and J. Enderlein, "Fast, background-free, 3D super-resolution optical fluctuation imaging (SOFI)," Proc. Natl. Acad. Sci. **106**(52), 22287–22292 (2009).
23. A. Sroda, A. Makowski, R. Tenne, U. Rossman, G. Lubin, D. Oron, and R. Lapkiewicz, "SOFISM: Super-resolution optical fluctuation image scanning microscopy," Optica **7**(10), 1308–1316 (2020).
24. C. J. R. Sheppard, M. Castello, G. Tortarolo, G. Vicidomini, and A. Diaspro, "Image formation in image scanning microscopy, including the case of two-photon excitation," J. Opt. Soc. Am. A **34**(8), 1339–1350 (2017).
25. C. J. R. Sheppard, M. Castello, G. Tortarolo, T. Deguchi, S. V. Koho, G. Vicidomini, and A. Diaspro, "Pixel reassignment in image scanning microscopy: a re-evaluation," J. Opt. Soc. Am. A **37**(1), 154–162 (2020).
26. M. Mishali and Y. C. Eldar, "Reduce and boost: Recovering arbitrary sets of jointly sparse vectors," IEEE Trans. Signal Process. **56**(10), 4692–4702 (2008).
27. Y. C. Eldar and G. Kutyniok, *Compressed Sensing : Theory and Applications* (Cambridge University, 2012).
28. Y. C. Eldar, *Sampling Theory Beyond Bandlimited Systems* (Cambridge University, 2015).
29. S. Gazit, A. Szameit, Y. C. Eldar, and M. Segev, "Super-resolution and reconstruction of sparse sub-wavelength images," Opt. Express **17**(26), 23920–23946 (2009).
30. Y. Shechtman, S. Gazit, A. Szameit, Y. C. Eldar, and M. Segev, "Super-resolution and reconstruction of sparse images carried by incoherent light," Opt. Lett. **35**(8), 1148–1150 (2010).
31. A. Szameit, Y. Shechtman, E. Osherovich, E. Bullkich, P. Sidorenko, H. Dana, S. Steiner, E. B. Kley, S. Gazit, T. Cohen-Hyams, S. Shoham, M. Zibulevsky, I. Yavneh, Y. C. Eldar, O. Cohen, and M. Segev, "Sparsity-based single-shot subwavelength coherent diffractive imaging," Nat. Mater. **11**(5), 455–459 (2012).
32. X. X. Zhu and R. Bamler, "A Sparse Image Fusion Algorithm With Application to Pan-Sharpening," IEEE Trans. Geosci. Remote Sens. **51**(5), 2827–2836 (2013).
33. W. Gong and S. Han, "High-resolution far-field ghost imaging via sparsity constraint," Sci. Rep. **5**(1), 9280 (2015).
34. O. Solomon, M. Mutzafi, M. Segev, and Y. C. Eldar, "Sparsity-based super-resolution microscopy from correlation information," Opt. Express **26**(14), 18238–18269 (2018).
35. U. Rossman, R. Tenne, O. Solomon, I. Kaplan-Ashiri, T. Dadosh, Y. C. Eldar, and D. Oron, "Rapid quantum image scanning microscopy by joint sparse reconstruction," Optica **6**(10), 1290–1296 (2019).
36. G. Dardikman-Yoffe and Y. C. Eldar, "Learned SPARCOM: unfolded deep super-resolution microscopy," Opt. Express **28**(19), 27736–27763 (2020).
37. Y. Israel, R. Tenne, D. Oron, and Y. Silberberg, "Quantum correlation enhanced super-resolution localization microscopy enabled by a fibre bundle camera," Nat. Commun. **8**(1), 14786 (2017).
38. S. Kurdzialek and R. Demkowicz-Dobrzanski, "Super-resolution Optical Fluctuation Imaging—fundamental estimation theory perspective," http://arxiv.org/abs/2009.01850.
39. M. Ingaramo, A. G. York, E. Hoogendoorn, M. Postma, H. Shroff, and G. H. Patterson, "Richardson-Lucy Deconvolution as a General Tool for Combining Images with Complementary Strengths," ChemPhysChem **15**(4), 794–800 (2014).
40. M. Guo, Y. Li, Y. Su, T. Lambert, D. D. Nogare, M. W. Moyle, L. H. Duncan, R. Ikegami, A. Santella, I. Rey-Suarez, D. Green, A. Beiriger, J. Chen, H. Vishwasrao, S. Ganesan, V. Prince, J. C. Waters, C. M. Annunziata, M. Hafner, W. A. Mohler, A. B. Chitnis, A. Upadhyaya, T. B. Usdin, Z. Bao, D. Colón-Ramos, P. La Riviere, H. Liu, Y. Wu, and H. Shroff, "Rapid image deconvolution and multiview fusion for optical microscopy," Nat. Biotechnol. **38**(11), 1337–1346 (2020).
41. S. Mallat, *A Wavelet Tour of Signal Processing* (Academic Press, San Diego, CA, 1999).
42. A. Beck and M. Teboulle, "A Fast Iterative Shrinkage-Thresholding Algorithm for Linear Inverse Problems," SIAM J. Imaging Sci. **2**(1), 183–202 (2009).
43. D. P. Palomar and Y. C. Eldar, *Convex Optimization in Signal Processing and Communications* (Cambridge University, 2010).

Optics EXPRESS

44. O. Solomon, Y. C. Eldar, M. Mutzafi, and M. Segev, "SPARCOM: Sparsity Based Super-resolution Correlation Microscopy," SIAM J. Imaging Sci. **12**(1), 392–419 (2019).
45. G. T. Dempsey, J. C. Vaughan, K. H. Chen, M. Bates, and X. Zhuang, "Evaluation of fluorophores for optimal performance in localization-based super-resolution imaging," Nat. Methods **8**(12), 1027–1036 (2011).
46. S. van de Linde and M. Sauer, "How to switch a fluorophore: from undesired blinking to controlled photoswitching," Chem. Soc. Rev. **43**(4), 1076–1087 (2014).
47. H. Li and J. C. Vaughan, "Switchable Fluorophores for Single-Molecule Localization Microscopy," Chem. Rev. **118**(18), 9412–9454 (2018).
48. K. Grußmayer, T. Lukes, T. Lasser, and A. Radenovic, "Self-Blinking Dyes Unlock High-Order and Multiplane Super-Resolution Optical Fluctuation Imaging," ACS Nano **14**(7), 9156–9165 (2020).
49. P. Dedecker, G. C. H. Mo, T. Dertinger, and J. Zhang, "Widely accessible method for superresolution fluorescence imaging of living systems," Proc. Natl. Acad. Sci. U. S. A. **109**(27), 10909–10914 (2012).
50. T. Dertinger, M. Heilemann, R. Vogel, M. Sauer, and S. Weiss, "Superresolution optical fluctuation imaging with organic dyes," Angew. Chemie - Int. Ed. **49**(49), 9441–9443 (2010).
51. M. Heilemann, S. van de Linde, M. Schüttpelz, R. Kasper, B. Seefeldt, A. Mukherjee, P. Tinnefeld, and M. Sauer, "Subdiffraction-Resolution Fluorescence Imaging with Conventional Fluorescent Probes," Angew. Chem., Int. Ed. **47**(33), 6172–6176 (2008).
52. T. Ha and P. Tinnefeld, "The Annual Review of Physical Chemistry is online at," Annu. Rev. Phys. Chem. **63**(1), 595–617 (2012).
53. J. J. Schmied, A. Gietl, P. Holzmeister, C. Forthmann, C. Steinhauer, T. Dammeyer, and P. Tinnefeld, "Fluorescence and super-resolution standards based on DNA origami," Nat. Methods **9**(12), 1133–1134 (2012).
54. A. Beck and M. Teboulle, "Fast gradient-based algorithms for constrained total variation image denoising and deblurring problems," IEEE Trans. Image Process. **18**(11), 2419–2434 (2009).
55. S. Jiang, Y. Zhang, H. Yang, Y. Xiao, X. Miao, R. Li, Y. Xu, and X. Zhang, "Enhanced SOFI algorithm achieved with modified optical fluctuating signal extraction," Opt. Express **24**(3), 3037–3045 (2016).
56. X. Yi, S. Son, R. Ando, A. Miyawaki, and S. Weiss, "Moments reconstruction and local dynamic range compression of high order superresolution optical fluctuation imaging," Biomed. Opt. Express **10**(5), 2430–2445 (2019).
57. N. Gustafsson, S. Culley, G. Ashdown, D. M. Owen, P. M. Pereira, and R. Henriques, "Fast live-cell conventional fluorophore nanoscopy with ImageJ through super-resolution radial fluctuations," Nat. Commun. **7**(1), 12471 (2016).
58. B. Wang, L. Yao, Y. Jing, Y. Fei, Q. Bai, L. Mi, and J. Ma, "Multicomposite super-resolution microscopy: Enhanced Airyscan resolution with radial fluctuation and sample expansions," J. Biophotonics **13**(5), e2419 (2020).
59. K. S. Grußmayer, S. Geissbuehler, A. Descloux, T. Lukes, M. Leutenegger, A. Radenovic, and T. Lasser, "Spectral cross-cumulants for multicolor super-resolved SOFI imaging," Nat. Commun. **11**(1), 3023 (2020).